The current issue and full text archive of this journal is available at
www.emeraldinsight.com/0961-5539.htm

Fast transient solution of a two-layered counter-flow microchannel heat sink

S.L. Beh and K.-K. Tio
Faculty of Engineering and Technology, Multimedia University, Melaka, Malaysia
G.A. Quadir
School of Mechatronics Engineering, Universiti Malaysia Perlis, Perlis, Malaysia, and
K.N. Seetharamu
PES Institute of Technology, Bangalore, India

Received 26 July 2007
Revised 10 June 2008
Accepted 30 June 2008

Abstract

Purpose – The purpose of this paper is to apply asymptotic waveform evaluation (AWE) to the transient analysis of a two-layered counter-flow microchannel heat sink.

Design/methodology/approach – A two-layered counter-flow microchannel heat sink in both steady state and transient conditions is analysed. Finite element analysis is used in the steady state analysis whereas AWE is used in the transient analysis.

Findings – A two-layered microchannel produces different temperature distribution compared to that obtained for a single-layered microchannel. The maximum temperature occurs at the middle of the bottom wall whereas the maximum temperature of a single-layered microchannel is at the outlet of the bottom wall. The time taken to reach steady state is also investigated for different coolant flow rate and heat flux boundary conditions. It is observed that when fluid velocity increases, the time taken to reach steady state decreases, however, when the heat flux increases, the time taken to reach steady state does not change.

Research limitations/implications – The fluid is incompressible and does not undergo phase change. The use of AWE provides an alternative method in solving heat transfer problem.

Practical implications – New and additional data will be useful in the design of a microchannel heat sink for the purpose of cooling of electronic components.

Originality/value – AWE is widely used in analyses of signal delays in electronic circuits, and rarely applied to mechanical systems. The present study applies AWE to heat transfer problems, and reveals that it reduces the computational time considerably. The results obtained are compared with conventional methods available in the literature, and they show good agreement. Hence the computational time is reduced, and the accuracy of results is verified.

Keywords Waveforms, Finite element analysis, Flow, Cooling, Electronic equipment and components
Paper type Research paper

1. Introduction

Microchannel (Figure 1) is used as heat sink for cooling the electronic packages as it has a high heat transfer coefficient. Tuckerman and Pease (1981) pioneered this idea of cooling to VLSI chips, where they fabricated the microchannel by etching it directly at the back of a silicon chip. A cover plate at the fin tips is used to confine the coolant in the channel, and to insulate heat flow. Subsequently, several researchers focused their analyses, either on the formulation of equations, hydrodynamic and thermodynamic aspects of the flow in microchannel (Philips, 1990; Wen and Choo, 1997), or the numerical methods for solving the governing equations (Copeland *et al.*, 1996; Quadir *et al.*, 2002). The performance of a microchannel is evaluated based on its ability to reduce the temperature of the system; hence some researchers (Harpole and Eninger, 1991; Knight *et al.*, 1992) shifted their focus

International Journal of Numerical Methods for Heat & Fluid Flow
Vol. 19 No. 5, 2009
pp. 595-616

0961-5539
DOI 10.1108/09615530910963544

to optimising the microchannel geometry to obtain the lowest temperature under specified flow conditions and heat flux.

In optimising the thermal performance of the microchannel, Vafai and Zhu (1999) introduced two-layered counter-flow microchannel (Figure 2), and their steady state result showed a substantial improvement in temperature reduction of the microchannel. Subsequently, Chong *et al.* (2002), Wei and Joshi (2003) and Jeevan *et al.* (2004) also investigated the two-layered counter-flow microchannel under steady state conditions using their own sets of equations, and their results also showed significant improvement compared to that for a single-layered microchannel.

The analyses of two-layered microchannel available in the literature focus only on steady state results. Thus the objective of the present paper is to perform a transient analysis of a two-layered counter-flow microchannel. The finite element analysis (FEA) is used to solve the governing equations of the system. In addition to that, a method named asymptotic waveform evaluation (AWE) is employed in the transient formulation. AWE was first introduced by Pillage and Rohrer (1990) for the analysis of delay of electronic signals. Liu *et al.* (1995) applied the AWE in the thermal analyses of electronic packages and printed circuit board. AWE has also been proven successful in the analysis of triple stack cold plate (Beh *et al.*, 2005), as well as in the single-layered microchannel (Ooi *et al.*, 2003).

2. Modeling and formulation

Figure 2 shows a two-layered microchannel in operation. However, for the purpose of analysing the complete channel, a simplified model, as shown in Figure 3, is analysed to save computational time and cost. Thus, Figure 3 is the model used in the present analysis after taking into consideration the symmetrical nature of microchannel geometry and the boundary conditions. Since the boundary conditions at top cover plate are not known exactly, we model the boundary as insulated. Hence the results we get are conservatively the upper bound values. Any dissipation from top will reduce the fluid exit temperature. The different walls of the proposed microchannel model along with the notations of the geometry and the coordinate axes are shown clearly in Figures 3 and 4. The domain is discretized into elements and nodes as shown in Figure 5. Figure 5 is considered as one unit cell representing the domain, which has 14 nodes. For better accuracy, the domain can be discretized into more than one unit cell, an example being Figure 6 where the domain is discretized into five unit cells.

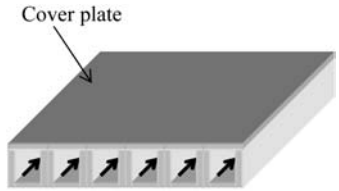

Figure 1.
Single-layered microchannel

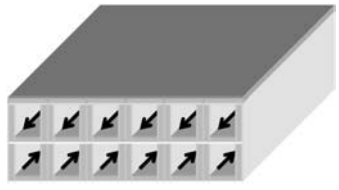

Figure 2.
Two-layered microchannel

The formulation of the microchannel analysis is divided into two major parts: physical and numerical. The physical formulation includes the governing equations of heat transfer from the wall (solid) as well as that from the fluid flowing in the channel. The numerical formulation is further divided into two parts: FEA and AWE.

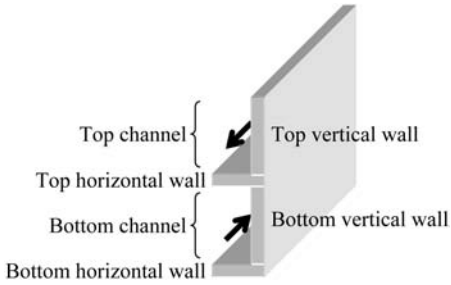

Figure 3.
A microchannel model used in present analysis

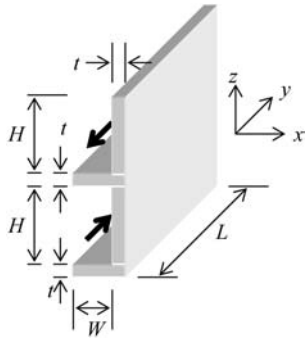

Figure 4.
Nomenclature of a microchannel model

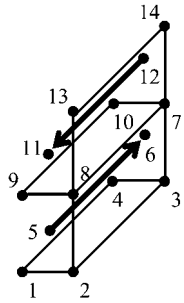

Figure 5.
One unit cell of a microchannel model

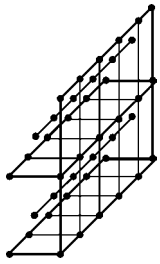

Figure 6.
A microchannel model discretized into five unit cells

2.1 Governing equations

Assuming the material of the wall is isotropic, the energy equations for all walls under transient conditions are derived based on the two-dimensional fins and are given in Equations (1)-(4).

$$\text{Top horizontal (t-h) wall: } k\frac{\partial^2 T}{\partial x^2} + k\frac{\partial^2 T}{\partial y^2} - \frac{h}{t}(T - T_{\text{f}})_{\text{t-h}} = \rho c\frac{\partial T}{\partial \tau} \quad (1)$$

$$\text{Bottom horizontal (b-h) wall: } k\frac{\partial^2 T}{\partial x^2} + k\frac{\partial^2 T}{\partial y^2} - \frac{h}{t}(T - T_{\text{f}})_{\text{b-h}} = \rho c\frac{\partial T}{\partial \tau} \quad (2)$$

$$\text{Top vertical (t-v) wall: } k\frac{\partial^2 T}{\partial y^2} + k\frac{\partial^2 T}{\partial z^2} - \frac{h}{t}(T - T_{\text{f}})_{\text{t-v}} = \rho c\frac{\partial T}{\partial \tau} \quad (3)$$

$$\text{Bottom vertical (b-v) wall: } k\frac{\partial^2 T}{\partial y^2} + k\frac{\partial^2 T}{\partial z^2} - \frac{h}{t}(T - T_{\text{f}})_{\text{b-v}} = \rho c\frac{\partial T}{\partial \tau} \quad (4)$$

where

k = wall thermal conductivity, W/m °C

h = heat transfer coefficient, W/m^2 °C

t = fin half thickness, m

c = wall specific heat, J/kg °C

ρ = wall density, kg/m^3

T = solid temperature, °C

T_{f} = fluid temperature, °C

x, y = spatial variable, m

τ = time variable, s

The heat transfer from the two vertical walls and the bottom wall to the fluid yields the following equations for the fluid.

$$\text{Top channel: } \dot{m}c_{\text{f}}\frac{\partial T_{\text{f}}}{\partial y} + \rho_{\text{f}}c_{\text{f}}WH\frac{\partial T_{\text{f}}}{\partial \tau} = hH(T - T_{\text{f}})_{\text{t-v}} + hW(T - T_{\text{f}})_{\text{t-h}} \quad (5)$$

Bottom channel:

$$\dot{m}c_{\text{f}}\frac{\partial T_{\text{f}}}{\partial y} + \rho_{\text{f}}c_{\text{f}}WH\frac{\partial T_{\text{f}}}{\partial \tau} = hH(T - T_{\text{f}})_{\text{b-v}} + hW(T - T_{\text{f}})_{\text{b-h}} + hW(T - T_{\text{f}})_{\text{t-h}} \quad (6)$$

where

$\dot{m}$ = fluid mass flow rate, assumed to be same for top and bottom channels, kg/s

c_{f} = fluid specific heat, J/kg °C

H = channel height, assumed to be same for top and bottom channels, m

w = channel width, assumed to be same for top and bottom channels, m

ρ_f = fluid density, kg/m^3

2.2 Finite element equations1

The wall is discretized into a two-dimensional bilinear rectangular element. Therefore, the temperature variation is assumed to be:

$$T = [N]\{T\} \tag{7}$$

where the shape functions are given by:

$$[N] = \left[1 - \frac{y}{L} - \frac{z}{H} + \frac{yz}{LH} \quad \frac{y}{L} - \frac{yz}{LH} \quad \frac{yz}{LH} \quad \frac{y}{H} - \frac{yz}{LH}\right] \tag{8}$$

if

$$\{T\} = \{\, T_2 \quad T_3 \quad T_7 \quad T_8 \,\}^{\mathrm{T}} \quad \text{or} \quad \{\, T_7 \quad T_8 \quad T_{13} \quad T_{14} \,\}^{\mathrm{T}}$$

or,

$$[N] = \left[1 - \frac{y}{L} - \frac{x}{W} + \frac{xy}{WL} \quad \frac{y}{L} - \frac{xy}{WL} \quad \frac{xy}{WL} \quad \frac{y}{H} - \frac{xy}{WL}\right] \tag{9}$$

if

$$\{T\} = \{\, T_1 \quad T_2 \quad T_3 \quad T_4 \,\}^{\mathrm{T}} \quad \text{or} \quad \{\, T_7 \quad T_8 \quad T_9 \quad T_{10} \,\}^{\mathrm{T}}$$

However, for the fluid, a one-dimensional linear element is considered. Hence, its temperature distribution is assumed to be:

$$T_f = [N]_f\{T\}_f \tag{10}$$

where the shape functions are given by:

$$[N]_f = [N_5 \;\; N_6] = \left[1 - \frac{y}{L} \quad \frac{y}{L}\right] \tag{11}$$

$$\{T\}_f = \{\, T_5 \quad T_6 \,\}^{\mathrm{T}} \quad \text{or} \quad \{\, T_{11} \quad T_{12} \,\}^{\mathrm{T}} \tag{12}$$

depending upon the channel being considered.

The different temperature differences as expressed in Equations (1) to (6) are given by:

$$(T - T_f)_{\text{t-h}} = \frac{1}{4}(T_7 + T_8 + T_9 + T_{10}) - \frac{1}{2}(T_{11} + T_{12}) \tag{13}$$

$$(T - T_f)_{\text{b-h}} = \frac{1}{4}(T_1 + T_2 + T_3 + T_4) - \frac{1}{2}(T_5 + T_6) \tag{14}$$

$$(T - T_f)_{\text{t-v}} = \frac{1}{4}(T_7 + T_8 + T_{13} + T_{14}) - \frac{1}{2}(T_{11} + T_{12}) \tag{15}$$

$$(T - T_f)_{b\text{-}v} = \frac{1}{4}(T_2 + T_3 + T_7 + T_8) - \frac{1}{2}(T_5 + T_6) \tag{16}$$

By using Galerkin's method, as explained in Segerlind (1984) and Lewis *et al.* (1996), the element stiffness matrices for the walls are obtained as follows:

Top and bottom vertical walls:

$$[\mathrm{EKM}] = \begin{bmatrix} \frac{tkH}{3L} + \frac{tkL}{3H} + \frac{hLH}{16} & -\frac{tkH}{3L} + \frac{tkL}{6H} + \frac{hLH}{16} & -\frac{hLH}{8} & -\frac{hLH}{8} \\ -\frac{tkH}{3L} + \frac{tkL}{6H} + \frac{hLH}{16} & \frac{tkH}{3L} + \frac{tkL}{3H} + \frac{hLH}{16} & -\frac{hLH}{8} & -\frac{hLH}{8} \\ -\frac{tkH}{6L} - \frac{tkL}{6H} + \frac{hLH}{16} & \frac{tkH}{6L} - \frac{tkL}{3H} + \frac{hLH}{16} & -\frac{hLH}{8} & -\frac{hLH}{8} \\ \frac{tkH}{6L} - \frac{tkL}{3H} + \frac{hLH}{16} & -\frac{tkH}{6L} - \frac{tkL}{6H} + \frac{hLH}{16} & -\frac{hLH}{8} & -\frac{hLH}{8} \end{bmatrix}$$
$$\begin{bmatrix} -\frac{tkH}{6L} - \frac{tkL}{6H} + \frac{hLH}{16} & \frac{tkH}{6L} - \frac{tkL}{3H} + \frac{hLH}{16} \\ \frac{tkH}{6L} - \frac{tkL}{3H} + \frac{hLH}{16} & -\frac{tkH}{6L} - \frac{tkL}{6H} + \frac{hLH}{16} \\ \frac{tkH}{3L} + \frac{tkL}{3H} + \frac{hLH}{16} & -\frac{tkH}{3L} + \frac{tkL}{6H} + \frac{hLH}{16} \\ -\frac{tkH}{3L} + \frac{tkL}{6H} + \frac{hLH}{16} & \frac{tkH}{3L} + \frac{tkL}{3H} + \frac{hLH}{16} \end{bmatrix} \tag{17}$$

Top and bottom horizontal walls:

$$[\mathrm{EKH}] = \begin{bmatrix} \frac{tkW}{3L} + \frac{tkL}{3W} + \frac{hLW}{16} & \frac{tkW}{6L} - \frac{tkL}{3W} + \frac{hLW}{16} & -\frac{tkW}{6L} - \frac{tkL}{6W} + \frac{hLW}{16} \\ \frac{tkW}{6L} - \frac{tkL}{3W} + \frac{hLW}{16} & \frac{tkW}{3L} + \frac{tkL}{3W} + \frac{hLW}{16} & -\frac{tkW}{3L} + \frac{tkL}{6W} + \frac{hLW}{16} \\ -\frac{tkW}{6L} - \frac{tkL}{6W} + \frac{hLW}{16} & -\frac{tkW}{3L} + \frac{tkL}{6W} + \frac{hLW}{16} & \frac{tkW}{3L} + \frac{tkL}{3W} + \frac{hLW}{16} \\ -\frac{tkW}{3L} + \frac{tkL}{6W} + \frac{hLW}{16} & -\frac{tkW}{6L} - \frac{tkL}{6W} + \frac{hLW}{16} & \frac{tkW}{6L} - \frac{tkL}{3W} + \frac{hLW}{16} \end{bmatrix}$$
$$\begin{bmatrix} -\frac{tkW}{3L} + \frac{tkL}{6W} + \frac{hLW}{16} & -\frac{hLW}{8} & -\frac{hLW}{8} \\ -\frac{tkW}{6L} - \frac{tkL}{6W} + \frac{hLW}{16} & -\frac{hLW}{8} & -\frac{hLW}{8} \\ \frac{tkW}{6L} - \frac{tkL}{3W} + \frac{hLW}{16} & -\frac{hLW}{8} & -\frac{hLW}{8} \\ \frac{tkW}{3L} + \frac{tkL}{3W} + \frac{hLW}{16} & -\frac{hLW}{8} & -\frac{hLW}{8} \end{bmatrix} \tag{18}$$

Similarly, the element capacitance matrices for the walls are also obtained as follows:

Top and bottom vertical walls:

$$[\mathrm{ECM}] = \frac{\rho ctHL}{36}\begin{bmatrix} 4 & 2 & 1 & 2 \\ 2 & 4 & 2 & 1 \\ 1 & 2 & 4 & 2 \\ 2 & 1 & 2 & 4 \end{bmatrix} \tag{19}$$

Top and bottom horizontal walls:

$$[\mathrm{ECH}] = \frac{\rho ctWL}{36}\begin{bmatrix} 4 & 2 & 1 & 2 \\ 2 & 4 & 2 & 1 \\ 1 & 2 & 4 & 2 \\ 2 & 1 & 2 & 4 \end{bmatrix} \tag{20}$$

Finally, these element matrices are combined to form a global equation as follows:

$$[\mathrm{C}]\left\{\frac{dT}{d\tau}\right\} + [\mathrm{K}]\{T\} = \{b\} \tag{21}$$

where [C] is the assembly of element capacitance matrices ([ECM] and [ECH]), while [K] is the assembly of element stiffness matrices ([EKM] and [EKH]). $\{b\}$ is the constant heat flux boundary conditions from the bottom horizontal wall.

2.3 Asymptotic waveform evaluation

The Laplace transform of Equation (21) is given as follows, where θ_0 refers to the initial condition of the system.

$$[\mathrm{C}]\{s\theta(s) - \theta_0\} + [\mathrm{K}]\{\theta(s)\} = \{b\} \tag{22}$$

Subsequent steps treat the boundary conditions and initial conditions in two separate solutions, which are then combined to give the final solution. This is equivalent to solving a control system, where the response of the system is represented by a combination of two independent responses, namely zero state response (ZSR) and zero input response (ZIR). These terms are also used in the present formulation.

The ZSR is evaluated by setting the initial condition of the system as zero. For the present analysis, this means the initial temperature of the walls is equal to the ambient temperature. Therefore, Equation (22) is simplified as follows.

$$(s[\mathrm{C}] + [\mathrm{K}])\{\theta(s)\} = \{b\} \tag{23}$$

Next, the Taylor Series expansion of $\theta(s)$ about $s = 0$ is evaluated in order to obtain the moments M_n which are defined in the following equation.

$$\theta(s) = \theta(0) + \frac{\theta'(0)s}{1!} + \frac{\theta''(0)s^2}{2!} + \frac{\theta'''(0)s^3}{3!} + \ldots = \sum_{n=0}^{\infty} M_n s^n \tag{24}$$

where $M_n = \dfrac{\theta^n(0)}{n!}$.

When $s = 0$, Equation (23) becomes $[K]\{\theta(0)\} = \{b\}$, and Equation (24) becomes $\{\theta(0)\} = M_0$. These two equations are combined to become $M_0 = [K]^{-1}\{b\}$. Thus, the first moment M_0 for ZSR is obtained.

In order to evaluate the second moment M_1 for ZSR, Equation (23) is differentiated once with respect to s, then by setting $s = 0$, we get $[K]\{\theta'(0)\} + [C]\{\theta(0)\} = 0$. Also, from Equation (24), when $n = 1$, $M_1 = \{\theta'(0)\}$. Thus, the second moment is obtained using the equation: $[K]M_1 = -[C]M_0$. Based on the same approach, the n-th moment M_n can be obtained from a general formula: $[K]M_n = -[C]M_{n-1}$ for ZSR.

The ZIR is evaluated by setting the forcing function of the system as zero. In terms of the present analysis, this means the heat flux of the microchannel is equal to zero. Therefore, Equation (22) is simplified as follows.

$$(s[C] + [K])\{\theta(s)\} - [C]\{\theta_0\} = 0 \tag{25}$$

Next, the Taylor Series expansion of $\theta(s)$ about $s = 0$ for ZIR is evaluated to obtain the moments M_n as defined in Equation (24). Also, when $s = 0$, Equation (25) becomes $[K]\{\theta(0)\} = [C]\{\theta_0\}$, and Equation (24) becomes $\{\theta(0)\} = M_0$. These two equations are combined to get $M_0 = [K]^{-1}[C]\{\theta_0\}$. Thus, the first moment M_0 for ZIR is obtained.

In order to evaluate the second moment M_1 for ZIR, Equation (25) is differentiated once with respect to s, then by setting $s = 0$, we get $[K]\{\theta'(0)\} + [C]\{\theta(0)\} = 0$. Also, from Equation (24), when $n = 1$, $M_1 = \{\theta'(0)\}$. Thus, the second moment is obtained using the equation: $[K]M_1 = -[C]M_0$. Based on the same argument, the n-th moment M_n can be obtained from a general formula: $[K]M_n = -[C]M_{n-1}$ for ZIR.

M_n is the n-th moment of all nodes. Since the actual interest is the moment of only one node, we extract the moments of that node for further calculations, instead of working with the moments of all nodes. Let m_n represent the moments generated from node i (the node of our interest). Thus, an equation similar to Equation (24) can be written to represent the response of one particular node of interest, as follows:

$$\theta(s) = m_0 + m_1 s + m_1 s^2 + \ldots + m_{2q-1} s^{2q-1} = \sum_{n=0}^{2q-1} m_n s^n \tag{26}$$

Equation (26) must be evaluated twice: for ZIR and ZSR separately. In Equation (26), the series is finite from 0 to the $(2q - 1)$-th moment. AWE matches these moments to a reduced order model by using Padé approximation up to q number of moments only, which is strictly a proper rational function, as given by:

$$\theta(s) = \frac{b_0 + b_1 s + b_2 s^2 + \ldots + b_{q-1} s^{q-1}}{1 + a_1 s + a_2 s^2 + \ldots + a_q s^q} \tag{27}$$

Therefore, Equations (26) and (27) are combined to obtain Equation (28).

$$m_0 + m_1 s + m_1 s^2 + \ldots + m_{2q-1} s^{2q-1} = \frac{b_0 + b_1 s + b_2 s^2 + \ldots + b_{q-1} s^{q-1}}{1 + a_1 s + a_2 s^2 + \ldots + a_q s^q} \tag{28}$$

After cross-multiplication, the coefficients of s on the left and right-hand side are equated. Thus, a set of linear algebraic equations can be written as follows:

$$m_0 a_q + m_1 a_{q-1} + m_2 a_{q-2} + \cdots + m_{q-1} a_1 + m_q = 0 \tag{29}$$

$$m_1 a_q + m_2 a_{q-1} + m_3 a_{q-2} + \cdots + m_q a_1 + m_{q+1} = 0 \tag{30}$$

$$m_2 a_q + m_3 a_{q-1} + m_4 a_{q-2} + \cdots + m_{q+1} a_1 + m_{q+2} = 0 \tag{31}$$

$$\vdots$$

$$m_{q-1} a_q + m_q a_{q-1} + m_{q+1} a_{q-2} + \ldots + m_{2q-2} a_1 + m_{2q-1} = 0 \tag{32}$$

Equations (29)-(32) are written in the following matrix form:

$$\begin{bmatrix} m_0 & m_1 & m_2 & \cdots & m_{q-1} \\ m_1 & m_2 & m_3 & \cdots & m_q \\ m_2 & m_3 & m_4 & \cdots & m_{q+1} \\ \vdots & \vdots & \vdots & \cdots & \vdots \\ m_{q-1} & m_q & m_{q+1} & \cdots & m_{2q-2} \end{bmatrix} \begin{Bmatrix} a_q \\ a_{q-1} \\ a_{q-2} \\ \vdots \\ a_1 \end{Bmatrix} = - \begin{Bmatrix} m_q \\ m_{q+1} \\ m_{q+2} \\ \vdots \\ m_{2q-1} \end{Bmatrix} \tag{33}$$

Equation (33) is solved for $\{a\}$, which are then used to find the roots p by the following equation:

$$\sum_{i=0}^{q} a_i p^i = 0, \text{ where } a_0 = 1 \tag{34}$$

The roots are then assembled in the following matrix in order to find the residues $\{k\}$.

$$\begin{bmatrix} p_1^{-1} & p_2^{-1} & p_3^{-1} & \cdots & p_q^{-1} \\ p_1^{-2} & p_2^{-2} & p_3^{-2} & \cdots & p_q^{-2} \\ p_1^{-3} & p_2^{-3} & p_3^{-3} & \cdots & p_q^{-3} \\ \vdots & \vdots & \vdots & \cdots & \vdots \\ p_1^{-q} & p_2^{-q} & p_3^{-q} & \cdots & p_q^{-q} \end{bmatrix} \begin{Bmatrix} k_1 \\ k_2 \\ k_3 \\ \vdots \\ k_q \end{Bmatrix} = - \begin{Bmatrix} m_0 \\ m_1 \\ m_2 \\ \vdots \\ m_{q-1} \end{Bmatrix} \tag{35}$$

The poles and residues are then assembled in Equation (36), which represents the reduced order approximation, where $I(s)$ depends on the nature of the input: ZSR can be considered as a step input, where $I(s) = 1/s$; ZIR can be considered as a pulse input, where $I(s) = 1$. It is worth mentioning that ZSR and ZIR have different sets of poles and residues.

$$\theta(s) = \sum_{n=0}^{2q-1} m_n s^n = \sum_{n=1}^{q} \frac{k_n}{s - p_n} I(s) \tag{36}$$

In each response, the corresponding poles and residues are evaluated and then the total response is evaluated by simply adding the solutions of both ZSR and ZIR. Equation (37) shows the total response in time domain after performing the inverse Laplace

transformation where the first summation term represents the solution for ZSR, while the second represents the solution for ZIR.

$$\theta(\tau) = \sum_{i=0}^{q} \frac{k_i}{p_i} (\exp(p_i \tau) - 1) + \sum_{i=0}^{q} k_i \exp(p_i \tau) \tag{37}$$

3. Hydrodynamic and thermodynamic analyses

Fluid flow in microchannel may cover a variety of flow and heat transfer regimes, such as developing laminar flow or fully developed laminar flow. Furthermore, the microchannel may be operated under different flow constraints, such as constant pressure drop of the fluid, constant volume flow rate of the fluid or constant pumping power acting on the fluid. The formulation described above requires the value of heat transfer coefficient, suitable for different flow constraints. Furthermore, the value of friction factor is also needed to express the pressure drop across the microchannel or to establish the flow regime if the pressure drop is known. Wen and Choo (1997) have explained the methods of calculating the friction factor and heat transfer coefficients for the above stated different flow constraints that are used in the present analysis.

A summary of the results obtained from the calculations according to Wen and Choo (1997) is given below. The dimensions of the microchannel follow those of Jeevan *et al.* (2004), where $H = 100$ μm, $W = 100$ μm, $L = 1$ cm and $t = 100$ μm. The fluid used is water and the wall material is silicon, thus the material properties used in the analysis are tabulated in Table I.

Following the method of Wen and Choo (1997), the hydrodynamic analysis is performed subject to the constant pressure drop constraint of 56.4 kPa. In this situation, the hydrodynamic properties like fluid velocity, Reynolds number and friction factor are calculated and tabulated in Table II.

The hydrodynamic properties of the lower and upper channel are the same since these channels have the same geometry. However, the thermodynamic properties of both channels are different, because the lower channel is subject to four walls

Table I.
Properties of material used in flow analysis of microchannel

Properties	Silicon (wall)	Water (fluid)
Thermal conductivity k, W/m °C	148	0.6
Specific heat c, J/kg °C	712	4179
Density ρ, kg/m^3	2,330	997
Dynamic viscosity μ, N s/m^2	–	0.00085

Table II.
Flow characteristics of microchannel subject to the pressure drop of 56.4 kPa

Properties	Lower channel		Upper channel
Pressure drop, kPa		56.4	
Fluid velocity, m/s		2.25	
Reynolds number		264	
Friction factor		0.0557	
Nusselt number	3.83		3.78
Heat transfer coefficient, W/m^2 °C	22,964		22,633

transferring heat, while the upper channel is only subject to three walls transferring heat (Philips, 1990). The differences are shown in Table II, where the lower channel has higher Nusselt number and heat transfer coefficient compared with the upper channel, as expected.

4. Results and discussions

The results of the present analysis are presented into two main parts: steady state results and transient results. The steady state results are compared with results presented by other researchers for the purpose of validation of the formulation carried out in the present analysis. After that, the transient results using AWE are presented, and are compared with the results obtained from the traditional finite element transient analysis. The results of parametric studies are also discussed subsequently.

4.1 Mesh sensitivity analysis and results verification

As in any other numerical analysis, mesh sensitivity analysis and results verification are essential matters. Mesh sensitivity analysis is important to ensure the results converge when the domain is discretized into more elements. After that, the present results are verified with the results obtained from other researchers, to show that the modeling (governing equation and numerical schemes) of the problem is correct.

Mesh sensitivity analysis is described in Table III, where the bottom and top channel fluid outlet temperature are used as the subject of analysis. It is found that the bottom channel fluid outlet temperature value converges to a value of 27.124, while the top channel fluid outlet temperature 22.061. Therefore, all analyses that follow use 30 unit cells as the model.

The results in present analysis are verified with the results obtained from Jeevan *et al.* (2004) and Chong *et al.* (2002), in the form of the thermal resistance. Thermal resistance is defined as the maximum temperature of the microchannel over the heat flux from the bottom horizontal wall. The maximum temperature is located at the left edge of the bottom horizontal wall, approximately 0.65 cm from the bottom channel inlet, as shown in Figure 10. The thermal resistance can be calculated based on this value, and is found to be 0.2289 K/W. This value is in good comparison with Jeevan *et al.* (2004) and Chong *et al.* (2002), as shown in Table IV. With this, the method used in present study is verified.

No. of unit cells	Bottom channel fluid outlet temperature, °C	Top channel fluid outlet temperature, °C
5	27.131	22.056
10	27.126	22.060
15	27.125	22.060
20	27.124	22.060
25	27.124	22.060
30	27.124	22.061

Table III. Mesh sensitivity analysis of the numerical scheme

	Present study	Jeevan *et al.* (2004)	Chong *et al.* (2002)
Thermal resistance, K/W	0.2289	0.2351	0.236

Table IV. Comparison of the thermal resistance with other literatures

4.2 Computational time

To show that AWE is fast in obtaining the transient results, we need to compare the CPU time of AWE with the conventional FEA. The comparison is only valid when both methods are run on the same computer, but the pattern of the results should remain the same if a different computer is used. Table V shows the comparison of CPU time between AWE and FEA, and it clearly indicates that AWE only takes a fraction of the time taken by the conventional FEA. The reason is that AWE gives the results of one node at one run, unlike the FEA where the whole domain is solved when the matrix equation is formed.

4.3 Steady state results

Figure 7 shows the steady state fluid temperature profile in the top and bottom channels along the stream. The fluid temperature at the bottom channel outlet is higher than the fluid temperature of the top channel outlet, with a difference of about four degrees. This is because heat is generated from the bottom horizontal wall, and is carried away primarily by the fluid in the bottom channel with a higher heat transfer coefficient. Figure 7 also shows that the temperature profile intersects at a location before the midpoint of the channel, meaning that the temperature profile is not symmetrical.

Figure 8 shows the steady state top and bottom vertical walls temperature profile along the stream in three positions: bottom ($z = 0$), centre ($z = H$) and top ($z = 2H$). It is observed that there is a common similarity: all three profiles show maximum

No. of unit cells	CPU time, s AWE	FEA
5	0.4	26
10	0.4	57
15	0.5	120
20	0.6	187

Table V.
Comparison of CPU time between AWE and FEA

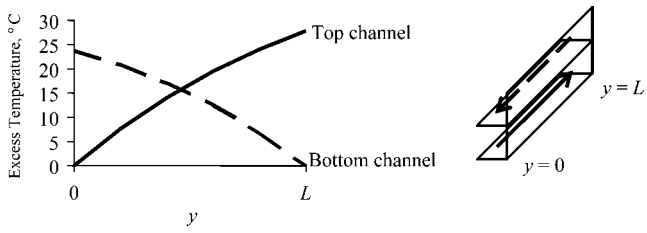

Figure 7.
Steady state fluid temperature in the top and bottom channels

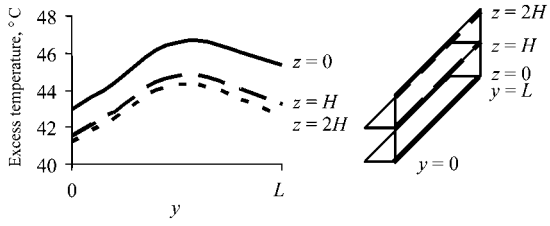

Figure 8.
Steady state top and bottom vertical walls temperature

temperature approximately at $y = L/2$, and decrease in the directions towards $y = 0$ and $y = L$. The wall temperature at $y = L$ is higher than the temperature at $y = 0$ irrespective of the positions $z = 0$, $z = H$ or $z = 2H$. This pattern is the result of counter flow nature of the fluid.

Figure 9 shows the steady state top and bottom horizontal walls temperature profile along the stream in two positions: left edge ($x = 0$) and right edge ($x = W$). In general, the bottom wall shows a higher temperature than the top wall. For the bottom wall, the left edge has a higher temperature than the right edge. Similar observation is found for the top wall. The reason is that the right edge transfers heat to the vertical wall in addition to the fluid in motion, while the left edge only dissipates heat to the fluid.

It is also observed in Figure 9 that the highest temperature of the microchannel wall is located at the left edge of the bottom horizontal wall, approximately 0.65 cm from the bottom channel inlet, as shown in Figure 10.

Figure 11 shows the steady state top and bottom vertical wall temperatures along the height of the channel inlet and outlet. It is seen from Figure 11 that the temperature decreases when the wall is farther away from the bottom horizontal wall. The rate of decrease is greater at the channel outlet as compared to that at channel inlet.

Figure 12 shows the steady state combined top and bottom vertical wall temperature. The high temperature region is at the middle bottom wall, with the maximum temperature occurring at $z = 0$, $y \approx 0.7L$, while the wall minimum temperature is at $y = 0, z = 2H$.

Figure 13 shows the steady state top horizontal wall temperature profile. The high temperature region takes a parabolic shape, slightly inclined to the top channel outlet

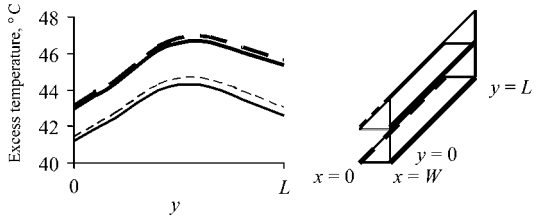

Figure 9.
Steady state top and bottom horizontal walls temperature

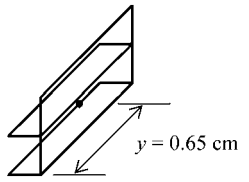

Figure 10.
Location of the maximum temperature of microchannel

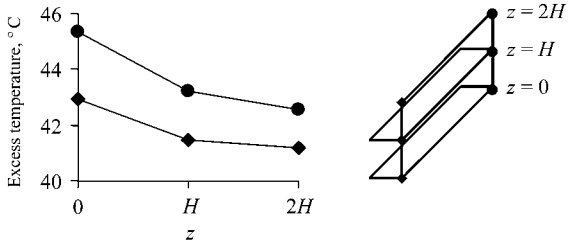

Figure 11.
Steady state top and bottom vertical wall temperatures at the channel inlet and outlet

($y = 0$), covers a wider area on $x = W$, and reduces towards $x = 0$. Figure 13 also shows that the temperature at $y = L$ is lower than at $y = 0$, meaning that the top horizontal wall is hotter near the outlet of top channel.

Figure 14 shows the steady state bottom horizontal wall temperature profile. The present profile is different from the top wall; the high temperature region is slightly inclined to the bottom channel outlet ($y = L$), covers a wider area on $x = 0$, and reduces towards $x = W$. Figure 14 also shows that the temperature at $y = 0$ is lower than at $y = L$, meaning that the bottom horizontal wall is hotter near the outlet of bottom channel.

4.4 Steady state parametric studies

This section focuses on the effect of changing the parameters of the system on the steady state temperature. Figure 15 shows the steady state fluid temperature profile in

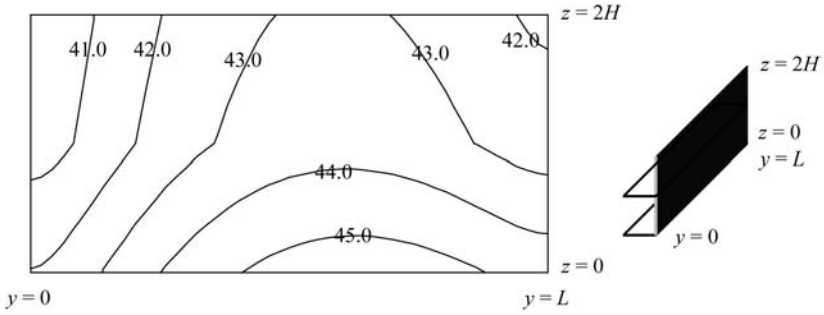

Figure 12.
Steady state combined top and bottom vertical wall temperature

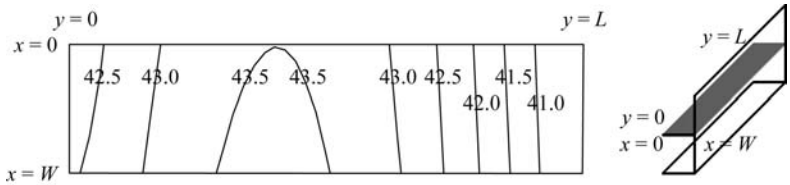

Figure 13.
Steady state top horizontal wall temperature

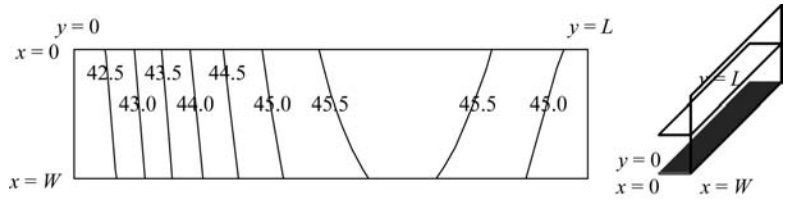

Figure 14.
Steady state bottom horizontal wall temperature

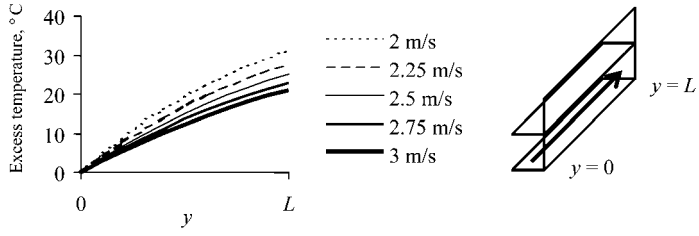

Figure 15.
Steady state fluid temperature profile in the bottom channel with different velocity

the bottom channel with velocity ranging from 2 to 3 m/s, while maintaining the fluid velocity of the top channel at 2.25 m/s. From Figure 15, we can see that when the fluid velocity increases, the overall temperature profile decreases. For clearer illustration, the temperature at the channel outlet are extracted and plotted in Figure 16.

Figure 16 shows the steady state fluid temperature at the outlet of the top and bottom channels as a function of fluid velocity ranging from 2 to 3 m/s. When the fluid velocity increases, the fluid temperature at both outlets decreases. However, the top channel always has a lower temperature than the bottom channel, which is consistent with the observation made from Figure 7.

Figure 17 shows the steady state maximum wall temperature as a function of fluid velocity ranging from 2 to 3 m/s. Expectedly, there is a decrease in the maximum wall temperature as the fluid velocity increases.

Figure 18 shows steady state fluid temperature profile in bottom channel with constant heat flux boundary conditions ranging from 100 to 400 W/cm^2. When the heat flux increases, the overall fluid temperature profile increases. The profile, however, is not linear along the channel.

Figure 19 shows steady state maximum wall temperature with different heat flux boundary conditions ranging from 100 to 400 W/cm^2. As expected, the maximum temperature obtained under steady state conditions increases with the increase in heat flux. However, it is noticed in this figure that the relationship between the maximum temperature and the heat flux is linear.

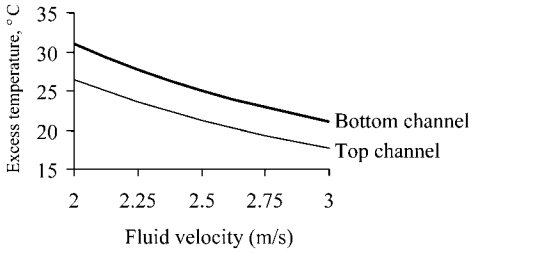

Figure 16.
Steady state fluid temperature at the outlet of the top and bottom channels

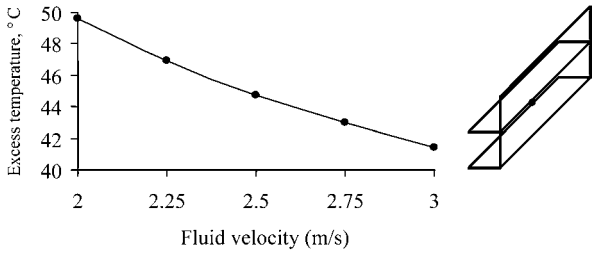

Figure 17.
Steady state maximum wall temperature with different fluid velocity

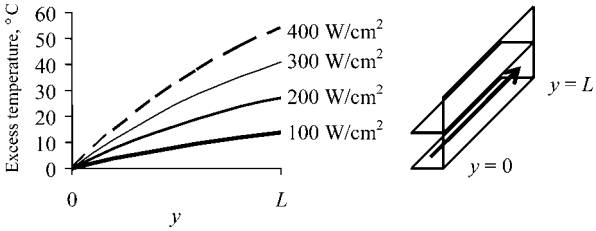

Figure 18.
Steady state fluid temperature profile in bottom channel with different heat flux

4.5 Transient results

The discussion of transient results begins with the comparison of results obtained from FEA with those obtained from AWE. Figure 20 shows the transient maximum wall temperature produced from FEA and AWE. It shows clearly that the results from AWE almost match with the results from FEA. This verifies all subsequent results using AWE that follow. Figure 20 also reveals that the time taken for the maximum temperature to reach steady state is approximately 0.03 s.

While explaining the method of AWE, it is noticed that the answer obtained depends upon the number of moments chosen in the analysis. An attempt is made in this regard to show the results of AWE in terms of the maximum wall temperature (Figure 21) using different values of moment. It is clear from Figure 21 that the result

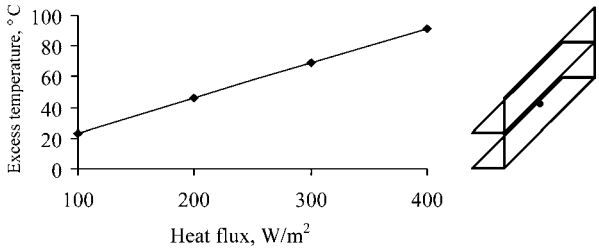

Figure 19.
Steady state maximum wall temperature with different heat flux

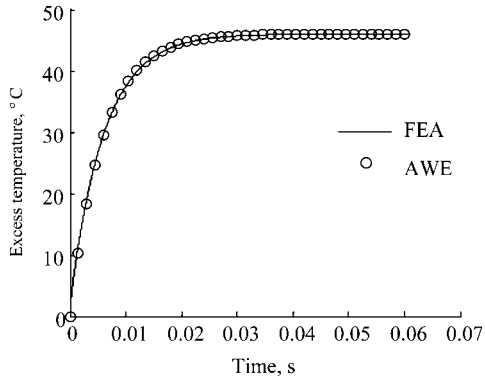

Figure 20.
Transient maximum wall temperature from FEA and AWE

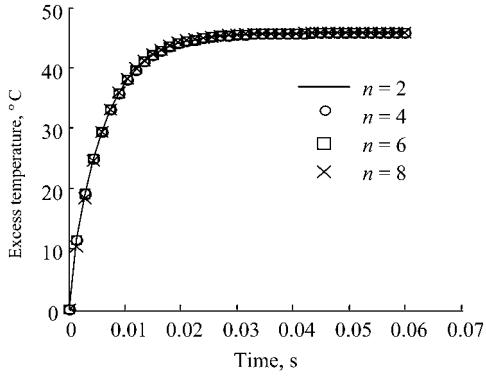

Figure 21.
Effect of number of moments in AWE on the accuracy of maximum wall temperature

using two moments is good enough to produce accurate results. Although higher number of moments also produces same results, the time taken to complete the calculation becomes relatively longer.

The fluid temperature profiles of bottom and top channels along the stream at different time are shown in Figures 22 and 23, respectively. The temperature profiles change rapidly at the initial stages. However, the change becomes gradual as the system approaches steady state.

Figure 24 shows the transient fluid temperature at the outlet of top and bottom channels. The estimated time for the fluid outlet temperature of the bottom channel to reach 99 percent of steady state temperature is approximately 0.02 s, while it also takes about 0.02 s for the outlet fluid temperature of the top channel to reach 99 percent of steady state temperature. This shows that both the fluids reach the steady state conditions almost at the same time.

Figure 25 shows transient combined top and bottom vertical wall temperature at intervals of 5 ms, starting from the top left at $t = 5$ ms. The series of figures show the high temperature region starts from the bottom, while the low temperature region falls on the top left of the wall. The temperature reaches steady state at approximately 60 ms, and the steady state profile matches with Figure 12.

Figure 26 shows a series of temperature profile of the top horizontal wall at the intervals of 10 ms, starting from the first figure on top left at $t = 10$ ms. This series of figures shows that the high temperature region forms at the middle of $x = W$ and spreads

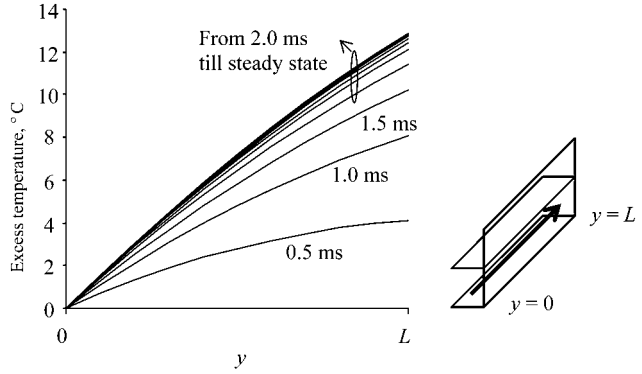

Figure 22.
Transient fluid temperature in the bottom channel

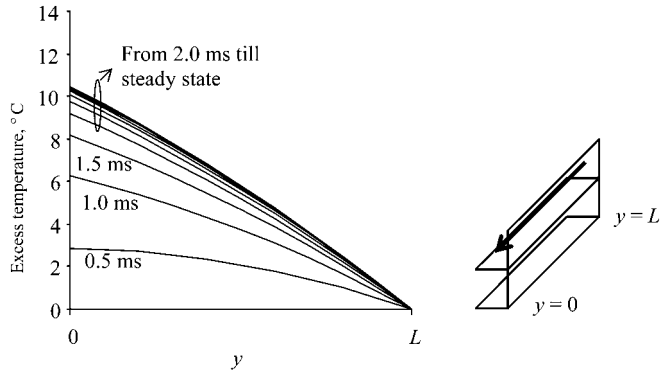

Figure 23.
Transient fluid temperature in the top channel

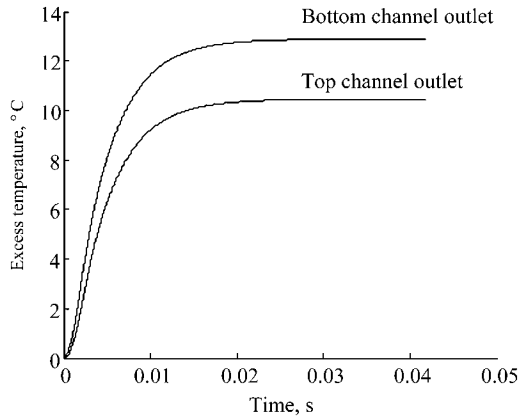

Figure 24.
Transient fluid temperature at the outlet of top and bottom channels

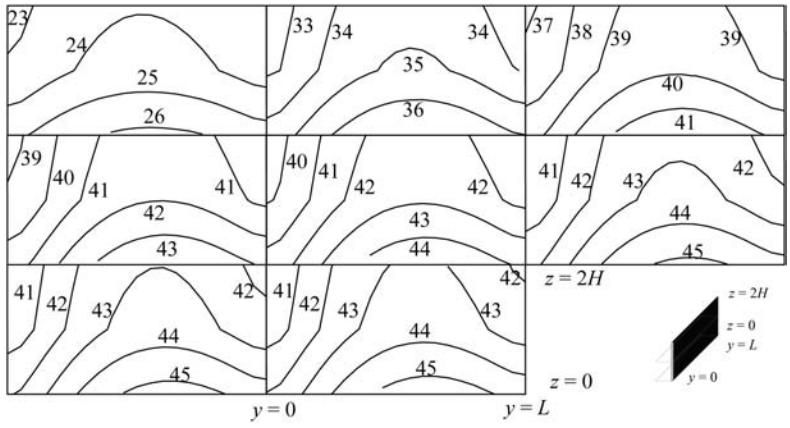

Figure 25.
Transient combined top and bottom vertical wall temperature

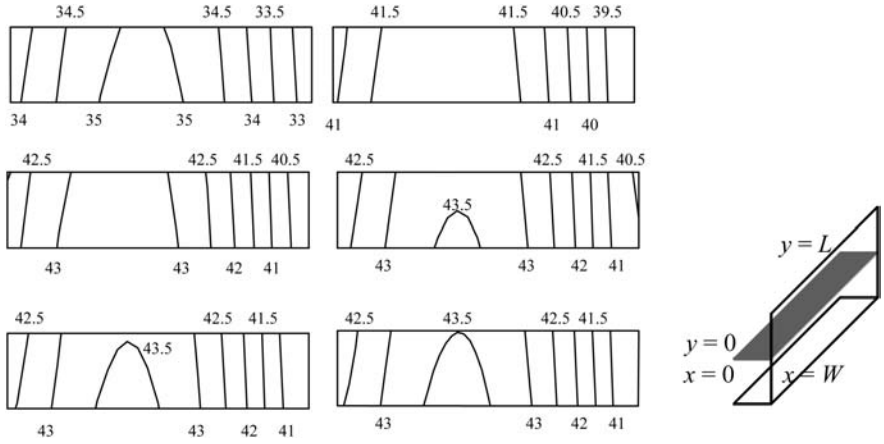

Figure 26.
Transient temperature profile of the top horizontal wall

out from here while the low temperature region always falls on $x = 0$, $y = L$. The parabolic high temperature region starts to be seen at 40 ms. The temperature reaches steady state at approximately 60 ms, and the steady state profile matches with Figure 13.

Figure 27 shows a series of temperature profile of the bottom horizontal wall at the intervals of 10 ms, starting from the first figure on top left at $t = 10$ ms. This series of figures shows that the high temperature region forms at the middle of $x = W$ and spreads out from here while the low temperature region always falls on the top left of the wall. The temperature reaches steady state at approximately 60 ms, and the profile is consistent with Figure 14.

4.6 Transient parametric studies

Figure 28 shows the transient fluid temperature at the outlet of bottom channel for fluid velocity ranging from 2 to 3 m/s. The steady state results are consistent with the results shown in Figure 13. Table VI shows that the time taken to reach steady state decreases as the fluid velocity increases.

Figure 29 shows the transient maximum wall temperature with different heat flux boundary conditions ranging from 100 to 400 W/cm^2. The steady state results are

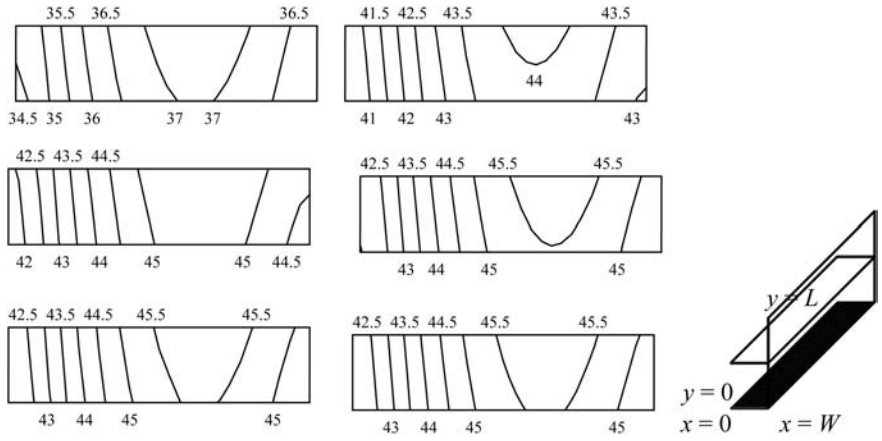

Figure 27.
Transient temperature profile of the bottom horizontal wall

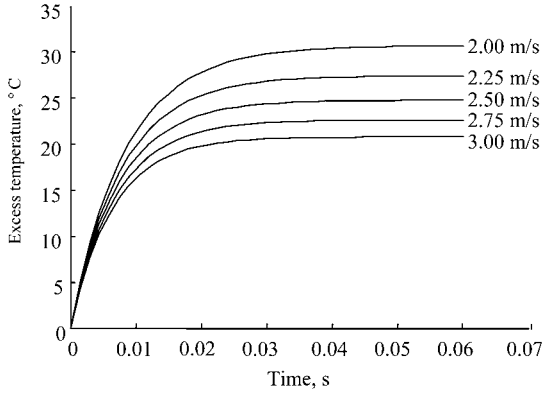

Figure 28.
Transient fluid temperature at the outlet of bottom channel with different fluid velocity

consistent with the results shown in Figure 18. Table VII, where values are extracted from Figure 29, shows that the time taken to reach steady state is almost constant at 13 ms even if the heat flux is increased.

5. Conclusions

The performance of a two-layered microchannel is analysed using FEA under steady and transient conditions. Also, AWE is used to obtain the transient behaviour of the same microchannel under the same operating conditions. Some parametric studies of the microchannel are also carried out in the present analysis. Based upon the above analyses, the following conclusions may be drawn:

- The result of AWE is verified with the result from FEA, and the computational time using AWE is very much less than FEA.
- The results of present analysis are verified with the results of other researchers, and shown to be close to the results of those researchers.

Table VI.
Steady state fluid outlet temperature and time taken to reach its 90 percent

Fluid velocity, m/s	Steady state lower channel fluid outlet temperature, °C	Time taken to reach 90% of steady state fluid outlet temperature, ms
2.00	31.1	21
2.25	27.8	19
2.50	25.1	18
2.75	22.9	17
3.00	21.0	16

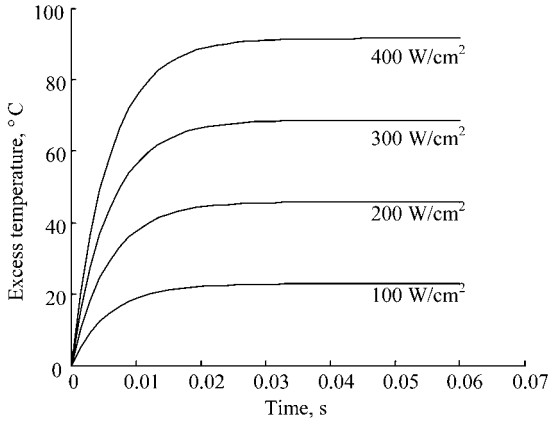

Figure 29.
Transient maximum wall temperature with different heat flux boundary conditions

Table VII.
Steady state maximum microchannel temperature and time taken to reach its 90 percent

Heat flux, W/cm^2	Steady state maximum temperature, °C	Time taken to reach 90% of steady state maximum temperature, ms
100	22.9	14
200	45.8	13
300	68.7	13
400	91.6	13

- The temperature profile of all walls (horizontal and vertical) along the flow shows a trend of increasing temperature towards the midpoint of channel, and a decreasing trend thereafter until the outlet of channel.
- The maximum temperature is located at the middle of the bottom horizontal wall, compared to the exit of the bottom horizontal wall in the case of a single-layered microchannel.
- The temperature at the outlet of bottom channel is higher than the outlet of top channel, because heat is generated from the bottom horizontal wall, and is carried away primarily by the fluid in the bottom channel with a higher heat transfer coefficient
- There is reduction in maximum temperature when the fluid velocity increases. Correspondingly, the time taken to reach steady state decreases as the fluid velocity increases.
- The maximum temperature increases when heat flux increases. However, the time taken to reach steady state is almost constant even though the heat flux increases.

References

Beh, S.L., Ooi, C.K., Quadir, G.A. and Seetharamu, K.N. (2005), "Steady and unsteady thermal analysis of a triple stack cold plate with heat losses", *International Journal of Numerical Methods for Heat & Fluid Flow*, Vol. 15, pp. 96-112.

Chong, S.H., Ooi, K.T. and Wong, T.N. (2002), "Optimisation of single and double layer counter flow microchannel heat sinks", *Applied Thermal Engineering*, Vol. 22, pp. 1569-85.

Copeland, D., Behnia, M. and Nakayama, W. (1996), "Manifold microchannel heat sinks, conjugate and extended analysis", *Proceedings of the 9th Symposium on Transport Phenomena in Thermal-Fluid Eng., Singapore*, pp. 498-503.

Harpole, G.M. and Eninger, J.E. (1991), "Microchannel heat exchanger optimization", *Proceedings of the 7th IEEE Semi-Therm Symposium*, pp. 59-63.

Jeevan, K., Azid, I.A. and Seetharamu, K.N. (2004), "Optimisation of double layer counter flow (DLCF) micro-channel heat sink used for cooling chips directly", *Proceedings of the Electronics Packaging Technology Conference, Singapore*, pp. 553-8.

Knight, R.W., Hall, D.J., Goodling, J.S. and Jaeger, R.C. (1992), "Heat sink optimization with application to microchannel", *IEEE Transactions on Components, Hybrids and Manufacturing Technology*, Vol. 15, pp. 832-42.

Lewis, R.W., Morgan, K., Thomas, H.R. and Seetharamu, K.N. (1996), *Finite Element Methods in Heat Transfer Analysis*, John Wiley & Sons, New York, NY.

Liu, D., Phanilatha, V., Zhang, Q. and Nakhla, M.S. (1995), "Asymptotic thermal analysis of electronic packages and printed circuit boards", *IEEE Transactions on Components, Packaging and Manufacturing Technology, Part A*, Vol. 18 No. 4, pp. 781-7.

Ooi, C.K., Seetharamu, K.N., Alauddin, Z.A.Z., Quadir, G.A., Sim, K.S. and Goh, T.J. (2003), "Fast transient solutions for heat transfer [FEM]", *TENCON 2003 Conference on Convergent Technologies for Asia-Pacific Region*, Vol. 1 Nos. 15-17, pp. 469-73.

Philips, R.J. (1990), "Microchannel heat sinks", *Proceedings of the Advances in Thermal Modeling of Electronic Components and Systems*, ASME Press, pp. 109-84.

Pillage, L.T. and Rohrer, R.A. (1990), "Asymptotic waveform evaluation for timing analysis", *IEEE Transaction on Computer Aided Design*, Vol. 9 No. 4, pp. 352-66.

Quadir, G.A., Beh, S.L., Seetharamu, K.N. and Hassan, A.Y. (2002), "A transient analysis of microchannel heat exchangers using the finite element method", *International Journal of Heat Exchangers*, Vol. III, pp. 67-88.

Segerlind, L.J. (1984), *Applied Finite Element Analysis*, John Wiley & Sons, New York, NY.

Tuckerman, D.B. and Pease, R.F.W. (1981), "High performance heat sink for VLSI", *IEEE Electron Device Letters*, Vol. 2 No. 5, pp. 126-9.

Vafai, K. and Zhu, L. (1999), "Analysis of two-layered micro-channel heat sink concept in electronic cooling", *International Journal of Heat and Mass Transfer*, Vol. 42, pp. 2287-97.

Wei, X. and Joshi, Y. (2003), "Optimization study of stacked micro-channel heat sinks for miceo-electronic cooling", *IEEE Trans. on Components and Packaging Technologies*, Vol. 26 No. 1, pp. 55-61.

Wen, Z. and Choo, K.F. (1997), "The optimum thermal design of microchannel heat sinks", *Proceedings of the IEEE/CPMT Electronic Packaging Technology Conference*, pp. 123-9.

Corresponding author
S.L. Beh can be contacted at: slbeh@mmu.edu.my